

Article

# Simulation of a Pulsed Metastable Helium Lidar

Jiaxin Lan <sup>1,2</sup> , Yuli Han <sup>1,2,\*</sup> , Ruocan Zhao <sup>1,2,3,4</sup> , Tingdi Chen <sup>1,2,3,4</sup>, Xianghui Xue <sup>1,2,3,4</sup> , Dongsong Sun <sup>1,2</sup>, Hang Zhou <sup>1,2</sup>, Zhenwei Liu <sup>1,2</sup> and Yingyu Liu <sup>1,2</sup>

- <sup>1</sup> School of Earth and Space Sciences, University of Science and Technology of China, Hefei 230026, China; lanjx@mail.ustc.edu.cn (J.L.); canlan@ustc.edu.cn (R.Z.); ctd@ustc.edu.cn (T.C.); xuexh@ustc.edu.cn (X.X.); sds@ustc.edu.cn (D.S.); spacezh@mail.ustc.edu.cn (H.Z.); lluzhen@mail.ustc.edu.cn (Z.L.); liuyingyu@mail.ustc.edu.cn (Y.L.)
- <sup>2</sup> CAS Key Laboratory of Geospace Environment, School of Earth and Space Sciences, University of Science and Technology of China, Hefei 230026, China
- <sup>3</sup> Anhui Mengcheng Geophysics National Observation and Research Station, University of Science and Technology of China, Hefei 230026, China
- <sup>4</sup> Hefei National Laboratory, University of Science and Technology of China, Hefei 230026, China
- \* Correspondence: hanyuli@ustc.edu.cn

**Abstract:** Measurements of atmosphere density in the upper thermosphere and exosphere are of great significance for studying space–atmosphere interactions. However, the region from 200 km to 1000 km has been a blind area for traditional ground-based active remote sensing techniques due to the limitation of facilities and the paucity of neutral atmosphere. To fulfill this gap, the University of Science and Technology of China is developing a powerful metastable helium resonance fluorescent lidar incorporating a 2 m aperture telescope, a high-energy 1083 nm pulsed laser, as well as a superconducting nanowire single-photon detector (SNSPD) with high quantum efficiency and low dark noise. The system is described in detail in this work. To evaluate the performance of the lidar system, numerical simulation is implemented. The results show that metastable helium density measurements can be achieved with a relative error of less than 20% above 370 km in winter and less than 200% in 270–460 km in summer, demonstrating the feasibility of metastable helium lidar.

**Keywords:** atmospheric optics; helium density lidar; resonance fluorescence; metastable helium; remote sensing



**Citation:** Lan, J.; Han, Y.; Zhao, R.; Chen, T.; Xue, X.; Sun, D.; Zhou, H.; Liu, Z.; Liu, Y. Simulation of a Pulsed Metastable Helium Lidar. *Photonics* **2024**, *11*, 465. <https://doi.org/10.3390/photonics11050465>

Received: 17 March 2024  
Revised: 7 May 2024  
Accepted: 13 May 2024  
Published: 15 May 2024



**Copyright:** © 2024 by the authors. Licensee MDPI, Basel, Switzerland. This article is an open access article distributed under the terms and conditions of the Creative Commons Attribution (CC BY) license (<https://creativecommons.org/licenses/by/4.0/>).

## 1. Introduction

The neutral atmosphere of the thermosphere and exosphere is closely related to space weather events, including variations in solar radiation intensity and geomagnetic activity. These changes can lead to significant disturbances in the thermosphere, profoundly affecting human space activities and exerting a substantial impact on space operations and ground-based technical systems. The thermosphere and exosphere are also the working altitudes of most applied satellites, so a change in atmospheric density in this region will affect the orbit stability and lifetime of satellites. Therefore, the monitoring and prediction of neutral atmospheric density in the thermosphere and exosphere is becoming increasingly important.

Traditional ground-based active remote sensing has struggled to penetrate the upper atmosphere, specifically the region spanning from 200 to 1000 km. This challenge stems from the constraints posed by existing facilities and the sparse nature of the neutral atmosphere in this zone. In this region, neutral atmosphere can be detected by space-borne, ground-based passive observation devices (such as FPI interferometers and gas-luminance imagers) and sounding rockets [1–3]. Rocket exploration is sporadic and is too exorbitant to obtain continuous data, whereas passive remote sensing techniques usually cannot acquire range-resolved observations. Lidar has demonstrated its ability to provide the high spatial and temporal resolution measurement of neutral densities, winds and temperatures in

the atmosphere [4–8]. Furthermore, lidar can fulfil the full seasonal and diurnal coverage of atmosphere measurements at much lower costs compared to rockets and satellites. Resonance fluorescence lidar has been successfully implemented with alkali metal atoms, such as sodium [9,10], iron [11,12] and potassium [13,14] in the mesosphere and lower thermosphere from 80 to 110 km. Due to the large backscattering cross-section of alkali metal atoms, which is approximately  $10^{14}$  times higher than the Rayleigh backscattering cross-section, and their longer average free path, resonance fluorescence is easily emitted. This resonance fluorescence signal can be used to determine the density of alkali metal atoms, as well as to measure wind fields and atmospheric temperatures. Similarly, in the thermosphere and exosphere, metastable helium is a suitable medium with a long lifetime and a large backscattering cross-section.

The helium fluorescence resonance lidar was initially proposed by Gerrard in 1997 [15]. Through a combination of passive experimental observations and theoretical simulations, it was demonstrated that this lidar is capable of obtaining metastable helium density within the altitude range of 400–700 km. A dozen years ago, Carlson et al. at the University of Illinois constructed a bistatic lidar system featuring a MOPA (Master Oscillator Power Amplifier) transmitter configuration, capable of delivering a 10 W single-mode, narrow-band continuous-wave (CW) laser [16]. This transmitter configuration was improved later to provide a 45 W CW laser [17]. The transmitted beam is imaged on the bistatic receiver, and the pixels of the array detector correspond to specific altitude range bins in the atmosphere. However, due to the limited range resolution and high integration difficulty of the bistatic system, a preference emerged for a monostatic pulsed lidar configuration. Kaifler et al. took a step in this direction by developing a helium lidar system at the German Aerospace Center. Their system employed a 0.5 W diode-pumped and Q-switched Nd:GdVO<sub>4</sub> laser, combined with a super-conducting nanowire single-photon detector, with which time-resolved measurements of metastable helium fluorescence have been achieved [18]. The obtained metastable helium density profiles exhibited a range resolution of 100 km and detection capabilities up to an altitude of up to 750 km. The profiles showed notable agreement with model predictions in terms of peak amplitude, peak altitude and the temporal evolution of density. The relative uncertainty arising from the various errors associated with the calibration process and with the pulse overlap was estimated to be around 30%.

In this paper, a metastable helium resonance fluorescence lidar system that utilizes a high-power 1083 nm pulsed laser and 2 m diameter telescopes is discussed. In the early stages of development, both pulsed-laser and CW lidar systems were considered. Ultimately, the pulsed lidar was preferred because of its ease of integration, high range resolution and shorter noise accumulation time [19,20]. With the advancements in 1083 nm pulsed laser technology, the decision was made to employ a pulsed lidar configuration. However, the augmentation of laser power introduces a severe saturation effect, which could potentially impact the performance of the lidar system. This paper comprehensively presents intricate details regarding the individual components of the lidar system and outlines the specific design implemented to cope with the saturation effect.

## 2. Fundamental Principles

The metastable helium in the thermosphere is mainly produced by the collision of ground-state helium atoms and photoelectrons (Equation (1)), along with the recombination of helium ions (Equation (2)), and is lost by photoionization (Equation (3)) at higher altitudes and the Penning effect (Equation (4)), where M stands for atoms such as O, N<sub>2</sub> and O<sub>2</sub>) at lower altitudes. Under the influence of a series of production, loss and transport mechanisms, metastable helium is mainly concentrated within the altitude range spanning from 400 to 700 km [21,22].





The collision of ground-state helium atoms and photoelectrons dominates the production of metastable helium. Consequently, when the thermosphere and exosphere are exposed to solar radiation, metastable helium becomes relatively abundant and can potentially be detected. However, the resonance fluorescence signal is quite weak and tends to be overwhelmed by strong background noise during daytime measurements. As a result, measurements of metastable helium density are best conducted during twilight hours.

Metastable helium has a considerable radiative lifetime of about 7870 s. This prolonged duration can be attributed to the forbidden transition from its metastable state ( $2^3S$ ) to the ground state ( $1^1S$ ), which makes metastable helium a viable candidate for resonance fluorescence [23].

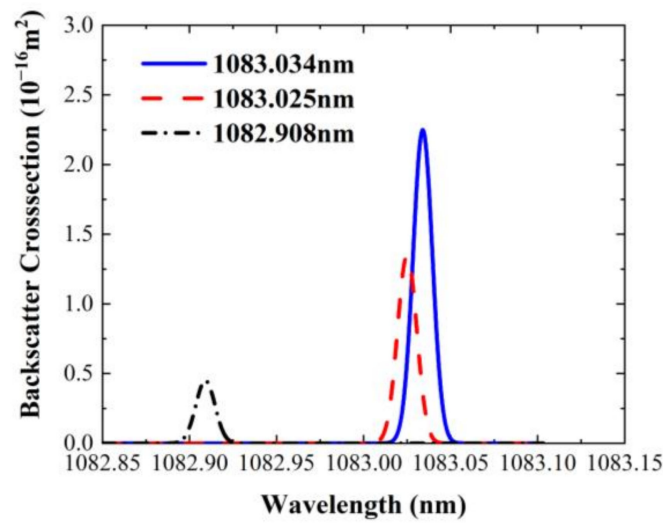
The 1083 nm, 388.9 nm and 318.8 nm lines observed from the airglow are generated by the transitions of helium in the thermosphere from  $2^3P$ ,  $3^3P$  and  $4^3P$  to  $2^3S$ , respectively [24]. Among these transitions, the 1083 nm radiation has a large Einstein coefficient and a backscattering cross-section comparable to that of alkali metals, which makes it easier to be detected, so 1083 nm is chosen as the wavelength of the resonance fluorescence lidar. The 1083 nm resonant radiation line of helium consists of three very close radiation lines of 1083.034 nm, 1083.025 nm and 1082.908 nm. This bandwidth of each radiation line is mainly determined by the natural linewidth, the collisional broadening and the Doppler broadening. Due to the low neutral atmosphere density in the upper atmosphere region, the collisional broadening can be neglected. The Doppler broadening linewidth for the typical temperature of 1125 K in the upper atmosphere region is about 3.3 GHz, which is much wider than the natural linewidth 1.6 MHz, so that the backscatter cross-section for each atomic transition line is given by the following:

$$\beta(\nu, \nu_0) = \frac{\sigma(\nu, \nu_0)}{4\pi} = \frac{\sigma_0}{4\pi} \exp\left(-\frac{(\nu(1 - V_R/c) - \nu_0)^2}{2\sigma_D^2}\right) \quad (5)$$

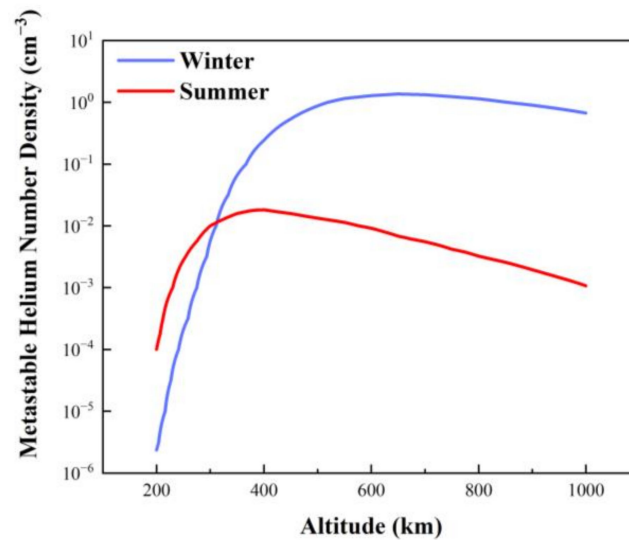
where  $\nu_0$  is the resonance frequency of each atomic transition line;  $\sigma(\nu, \nu_0)$  is the absorption intensity of each radiation line;  $\sigma_0$  is the peak absorption cross-section at resonance;  $V_R$  is vertical wind speed;  $\sigma_D$  is the rms linewidth of Doppler broadening,  $\sigma_D = \nu_0 \sqrt{\frac{k_B T}{Mc^2}}$ , where the  $k_B$  is the Boltzmann Constant,  $M$  is the mass of the helium and  $T$  is the temperature.

Figure 1 illustrates their respective backscattering cross-sections, with the data derived under the condition of a thermosphere temperature of 1125 K and a vertical wind speed of 0. Notably, the 1082.908 nm line is distant from the center of the three lines, and it features relatively small backscattering cross-sections. As a result, the primary focus for detection purposes is on the 1083.025 nm and 1083.034 nm lines [25].

The metastable helium density profile shown in Figure 2 is derived from a model established by Waldrop et al. in 2005, which is based on incoherent scattering radar observations at Arecibo Observatory [26]. The atmospheric pressure difference caused by the temperature difference between the winter and the summer hemisphere induces the transport of helium particles from the summer hemisphere to the winter hemisphere. Consequently, this leads to a heightened density of ground-state helium atoms in the thermosphere of the winter hemisphere. At the same time, the conjugated hemisphere experiences an enhanced influx of light during winter, contributing an augmented supply of conjugate photoelectrons. Given that metastable helium in the thermosphere predominantly forms through the collision of ground-state helium atoms and photoelectrons, the density of metastable helium in the thermosphere tends to be higher during winter, while being comparatively lower during summer in relation to other seasons.



**Figure 1.** Backscattering cross-section of metastable helium (vertical wind speed is 0 and temperature is 1125 K).



**Figure 2.** Metastable helium number density profiles in winter and summer seasons for the Arecibo Observatory in Puerto Rico from model established by Waldrop et al. [26].

### 3. System Structure

The metastable helium lidar based on a pulsed laser mainly consists of a laser-transmitting system, receiving system and acquisition system. The laser-transmitting system is used to emit a 1083 nm laser pulse to excite the metastable helium in the upper thermosphere and exosphere to the upper state. The receiver and acquisition system is used to receive and collect the metastable helium resonance fluorescence scattering signal from 200 km to 1000 km. The schematic optical layout of the system structure is shown in Figure 3.

In the transmitting optical system, the optical parametric generator (OPG) and optical parametric amplifier (OPA) system is employed. Beams from the OPG and OPA systems exhibit diameters of 10 mm. A beam-expanding system with a factor of 30 is employed to enlarge the beam diameter to 300 mm. Furthermore, the system serves to diminish the divergence angle from 1 mrad to a mere 33  $\mu$ rad.

The receiving system is an afocal reflective structure, comprising a primary mirror and a secondary mirror, with a diameter of 2 m and 100 mm, respectively. The received signal is collected by a fiber with NA of 0.22 and a core diameter of 200  $\mu$ m, which makes

the FOV of telescope 44  $\mu\text{rad}$ . A combination of an interference filter and a Fabry–Perot interferometer (FPI) with a diameter of 50 mm plays a vital role in mitigating background noise and enhancing the signal-to-noise ratio (SNR). After that, through a lens with a focal length of 104.8 mm, light is received by a fiber with a diameter of 200  $\mu\text{m}$  and an NA of 0.22, which is coupling with the detector.

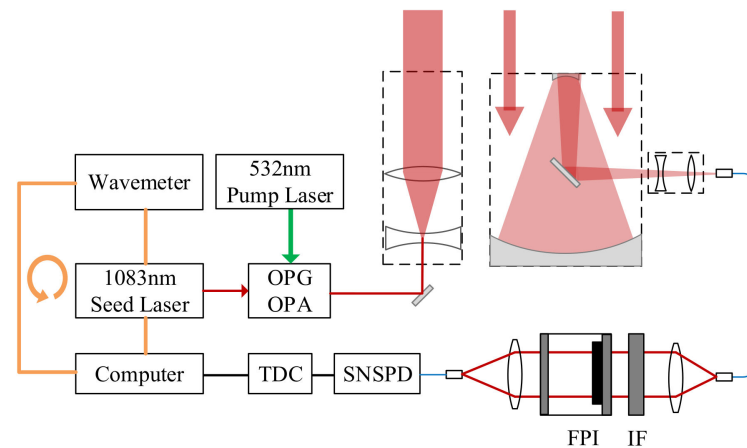


**Figure 3.** Schematic optical layout of metastable helium lidar (IF: interference filter; FPI: Fabry–Perot interferometer; SNSPD: superconducting nanowire single-photon detector; TDC: time-dependent single-photon counter; orange circle: PID loop).

### 3.1. Laser

To achieve a high-power and narrow linewidth laser at 1083 nm, the optical parametric generator (OPG) and optical parametric amplifier (OPA) system is employed. The system is designed to generate a tunable laser through the exploitation of nonlinear optical effects, allowing for the conversion of laser frequency through energy exchange within the medium. The chosen medium for these processes is potassium titanium oxide phosphate (KTiOPO<sub>4</sub>, KTP), renowned for its substantial nonlinear coefficient, superior thermal conductivity, and impressive damage threshold [27]. In this setup, KTP crystals serve as the medium and are stimulated by the second-harmonic, 532 nm laser emitted by an injection-seeded Nd:YAG laser. This interaction results in the release of a signal laser at 1083 nm and an idler laser at 1045 nm.

To ensure the stability of the emitting laser frequency, the PID (Proportional–Integral–Differential) control algorithm is employed. This control approach guarantees precise control over the laser frequency by factoring in three key components: proportionality, integration and differentiation. The real-time laser frequency is continuously measured using a wavemeter and then transmitted to a computer via a serial port. The PID algorithm operates by comparing the real-time frequency to a predefined set point and generating a frequency-adjustment signal that is conveyed to the seed laser, thereby correcting any detected frequency deviation.

As illustrated in Figure 4, over a 2 h measurement period, the effectiveness of the PID control algorithm is evident, as the frequency of the seed laser remains stable within a margin of 20 MHz. This robust control mechanism ensures the consistent and accurate emission of laser frequency, a critical element in maintaining the desired performance and stability of the system.

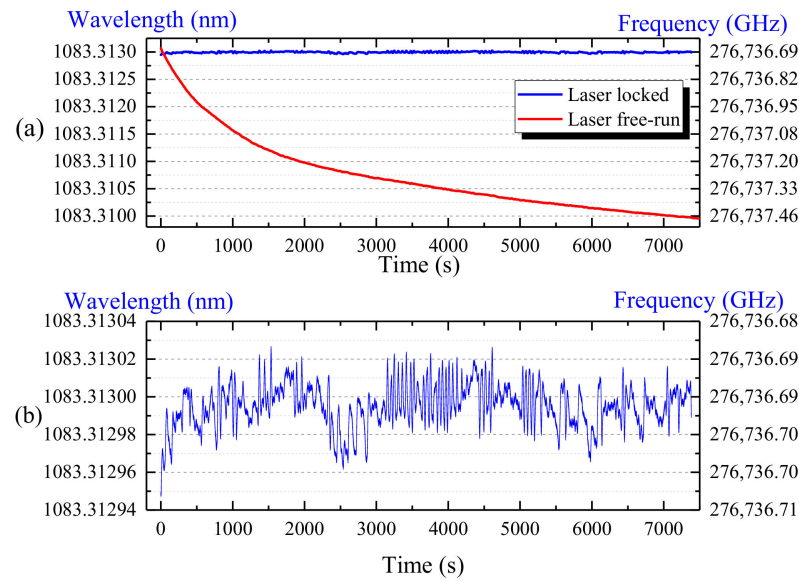


**Figure 4.** Frequency stability of seed laser in 2 h. Blue line and red line in (a) are frequency of seed laser with and without stabilized, respectively, and (b) is locked frequency in detail.

### 3.2. Filter

The 1083 nm backscatter resonance fluorescence received by telescopes appears considerably weak in comparison to sky background noise, which makes it a challenge to extract resonance fluorescence from the received signal. Consequently, the implementation of a robust filter system becomes pivotal, aimed at mitigating noise and augmenting the signal-to-noise ratio.

To address this concern, a customized narrow-band interference filter with a bandwidth of 0.5 nm and a peak transmittance of 99% is employed. However, the spectral width of the targeted transition lines around 1083 nm, considering Doppler broadening, extends to approximately 3.3 GHz, which is significantly smaller than the 0.5 nm provided by the narrow-band interference filter (equivalent to roughly 127 GHz at 1083 nm). This discrepancy underscores the necessity for an additional solution, which is where the FPI comes into play.

An FPI consists of two partially reflecting parallel mirrors, positioned a fixed distance apart within an optical cavity. Rooted in multi-beam interference theory, certain wavelengths of light will resonate within the cavity and get transmitted. The Free Spectral Range (FSR) of an FPI represents the separation in wavelength between consecutive transmission peaks in its transmittance spectrum. It is determined by the spacing between the mirrors and is an essential parameter for the device’s performance. The finesse of the FPI, determined by the quality of its coatings, as well as the flatness and parallelism of its component plates, is quantified by the ratio of FSR to Full Width at Half Maximum (FWHM).

The composite filter system consists of the narrow-band filter in conjunction with the FPI, effectively curbing background noise. The transmittance profile, illuminating the system’s filtering capability, is visually presented in Figure 5.

In addition to FPI, the Faraday anomalous dispersion optical filter (FADOF) presents an alternative option for filtering specific wavelengths of light. The FADOF technique has been developed for a variety of atoms, including Na, K, Rb and others. It exploits the Zeeman effect, where the spectral lines of atoms split when subjected to a magnetic field. The basic principle of the FADOF involves the interaction of linearly polarized light with an atomic medium in the presence of a magnetic field. As the light traverses the atomic medium parallel to the magnetic field, it decomposes into two circularly polarized components—left-hand and right-hand circular polarization—with different refractive indices and propagation speeds. This phenomenon, known as Faraday anomalous dispersion, causes the plane of polarization of the transmitted light to rotate as it propagates

through the medium. By adjusting parameters like the magnetic field intensity, temperature and propagation distance, it is possible to ensure that the plane of polarization of the incident light rotates by odd multiples of  $\pi/2$ . Consequently, light with frequencies away from the atoms' resonance frequency experiences rotation and can be blocked by orthogonal polarizers.

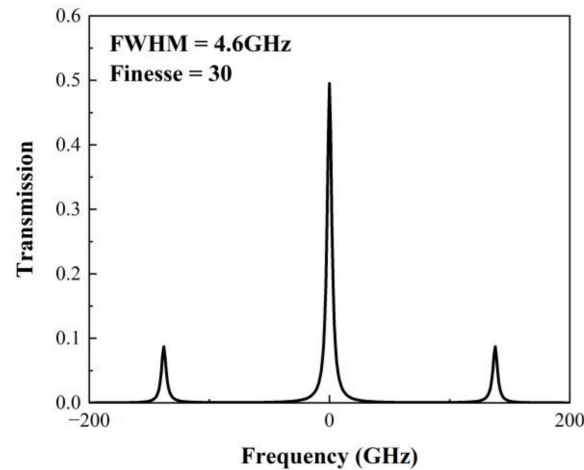


**Figure 5.** Simulated transmittance of the combination of interference filter and FPI.

An FADOF for metastable helium has been studied [28]. Under specific conditions, including a magnetic field strength of 230 Gs, helium cell charging pressure of 110 Pa and a helium cell length of 3 cm, the transmission curve exhibits two distinct flat peaks with transmission percentages of 32% and 57%, as shown in Figure 6.

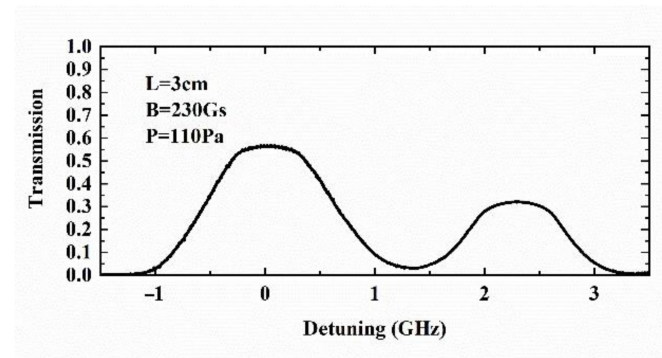


**Figure 6.** Transmission of FADOF.

### 3.3. Detector

The SNSPD (superconducting nanowire single-photon detector) has been widely used on lidars in recent years due to its high quantum efficiency, low dark current and low time jitter. The core component of the SNSPD is a narrow superconducting nanowire made of NbN (niobium nitride), which can be cooled to extremely low temperatures to achieve superconductivity. The interaction of a photon with the nanowire triggers the localized disturbance of the superconducting state, causing the nanowire to transfer into a resistive state. This transformation generates a voltage pulse that can be accurately measured and amplified, facilitating the detection of single photons.

The SNSPD integrated into this lidar system has been developed by Zhang Labao's group in Nanjing University [29,30]. The crucial requirement of maintaining the nanowire's superconducting state at extremely low temperatures is accomplished through the use of high-pressure helium. Remarkably, this SNSPD exhibits a quantum efficiency of 30% at 1083 nm, along with a low dark current rate of 800 cps. The active detection area of 60  $\mu\text{m}$

× 60 μm is arranged in a 2 × 2 array, with each individual pixel spanning 30 μm × 30 μm. The saturation counting rate for each pixel is within the range of 40–50 MHz. To interface with the lidar system, the SNSPD is optically coupled with a multimode fiber characterized by a diameter of 200 μm and an NA of 0.22.

#### 4. Simulations and Error Analysis

##### 4.1. Lidar Equation and Calibration

Metastable helium number density can be derived from the intensity of lidar return signal and lidar equation [25], which is shown as follows:

$$N_{He}(z) = \left[ \frac{P_L \tau}{hc/\lambda_0} \right] \cdot \left[ \sigma_{eff} n_{He}(z) \Delta z_{He} R_B \right] \cdot \left[ \frac{A_R}{4\pi z^2} \right] \cdot \left[ \eta T_a^2 E^2(z) G(z) \right] + \frac{2N_B \tau \Delta z_{He} f}{c} \quad (6)$$

where  $N_{He}(z)$  is photon counts measured by the detector in the range interval  $(z - \Delta z/2, z + \Delta z/2)$ .  $P_L$  is the power of the laser;  $\tau$  is cumulative time;  $f$  is the laser repetition frequency;  $hc/\lambda_0$  is the energy of a single photon;  $\sigma_{eff}$  is the effective scatter cross-section;  $n_{He}(z)$  is the number density of metastable helium;  $R_B$  is the branching ratio;  $A_R$  is the effective area of the telescope;  $\eta$  is the efficiency of the optical system;  $T_a$  is the one-way lower atmospheric transmittance;  $E(z)$  is the one-way extinction coefficient, which is due to the absorption of the metastable helium layer and can be calculated as  $E(z) = \exp(-\int_{z_{bottom}}^z \sigma_{eff}(z) n_{He}(z) dz)$ , where  $z_{bottom}$  is the bottom altitude of the metastable helium layer, and due to the paucity of helium density, the extinction is negligible, and thus,  $E(z) \approx 1$  in this case;  $G(z)$  is the geometry factor, which is assigned a value of 1 as geometric correction is not taken into consideration in the study.  $N_B$  is the background noise per second caused by solar radiation and the dark 273–274 current of detectors, etc.

On the right side of Equation (6), the first parenthesis term is the photon number emitted by the laser. The second parenthesis term is the probability that a photon is backscattered by the scatters, which are metastable helium atoms in this case. The third and the fourth parenthesis terms are the probability that a scattered photon is received by the telescope.

The signal-noise ratio (SNR) can be calculated by the following equation:

$$SNR(z) = \frac{N_{He}(z) - 2N_B \tau \Delta z_{He} f / c}{\sqrt{N_{He}(z)}} \quad (7)$$

However, the absolute metastable helium number density cannot be obtained directly from the lidar equation due to the uncertainty in laser power, atmosphere transmission, optical efficiency, etc. A commonly used method for solving the lidar equation is to use the Rayleigh scattering signal at a lower altitude as a reference and normalize the metastable helium resonance fluorescence signal to it. The Rayleigh scattering signal also follows the lidar equation and relates to the absolute atmosphere number density, which can be adopted from atmospheric models. Thus, the absolute metastable helium number density can be derived as follows:

$$n_0(z) = n_R(z_R) \frac{N_{He}(z) - 2N_B \tau \Delta z_{He} f / c}{N_R(z_R) - 2N_B \tau \Delta z_R f / c} \frac{z^2}{z_R^2} \frac{4\pi\sigma_R}{\sigma_{eff} R_B} \frac{\Delta z_R}{\Delta z} \frac{1}{E^2(z)} \quad (8)$$

where  $n_R(z_R)$  is the atmosphere number density at altitude  $z_R$ ,  $N_R(z_R)$  is the Rayleigh scattering photon counts,  $\sigma_R$  is the Rayleigh backscatter coefficient and  $\Delta z_R$  is the range resolution of Rayleigh scattering measurements.

##### 4.2. Saturation Effect

Due to the finite lifetime of the excited state of helium, a significant depopulation of metastable-state atoms occurs when the laser energy density is large enough [31–34]. In the meantime, the population of the excited state rises, leading to an increased rate of

stimulated emission and also a reduced rate of spontaneous emission. The stimulated emission cannot be backscattered and detected, while spontaneous emission can, causing a reduction in backscattered photon counts and an underestimation of metastable helium number density.

The parameters of the emitting system, such as laser pulse energy, pulse duration and divergence angle, directly determine the laser energy density, which further affects the saturation effect. Therefore, under specified pulse duration and divergence angle conditions, we optimized the laser pulse energy to minimize the saturation effect.

During the laser pulse duration  $\Delta t_L$ , the excited-state population  $n_e$  and the ground-state population  $(n - n_e)$  are not in the steady state due to absorption, spontaneous emission and stimulated emission.  $n_e$  can be determined by the rate equation as shown below:

$$\frac{dn_e}{dt} = -\frac{n_e}{\tau_R} + (n - n_e)\frac{\sigma_{eff}N_L(t)T}{z^2\Omega} - n_e\frac{\sigma_{eff}N_L(t)T}{z^2\Omega} \tag{9}$$

where  $\tau_R$  is the radiative lifetime of the excited state;  $n$  is the total number density of the atoms in the layer;  $N_L(t)$  is the total number of laser-emitted photons per unit time;  $T$  is the one-way atmosphere transmission;  $\Omega$  is the solid angle and related to the full divergence of laser beam  $\theta_L$  by the following:

$$\Omega = \frac{\pi}{4}\theta_L^2 \tag{10}$$

Assuming the temporal shape of the laser pulse is rectangular shape with a width of  $\Delta t_L$ , the following is obtained:

$$N_L(t) = \begin{cases} N_L/\Delta t_L, & 0 < t < \Delta t_L \\ 0, & t > \Delta t_L \end{cases} \tag{11}$$

where  $N_L$  is the total number of emitted photons during a pulse and can be expressed as  $N_L = \frac{p_L}{hc/\lambda_0}$ , where  $p_L$  is pulse energy. By solving Equation (9), the excited-state population is given by the following:

$$n_e(t) = \begin{cases} \frac{n\tau'}{2t_S}(1 - e^{-t/\tau'}) & t < \Delta t_L \\ \frac{n\tau'}{2t_S}(1 - e^{-\Delta t_L/\tau'})e^{-(t-\Delta t_L)\tau_R} & t > \Delta t_L \end{cases} \tag{12}$$

where  $t_S$  and  $\tau'$  are defined as follows:

$$t_S = \frac{z^2\Omega\Delta t_L}{2\sigma_{eff}N_LT_a} \tag{13}$$

$$\frac{1}{\tau'} = \frac{1}{\tau_R} + \frac{1}{t_S} \tag{14}$$

Since the decay rate of the excited-state population through spontaneous emission is  $n_e(t)/\tau_R$ , the number of reemitted photons per unit time in the volume considered will be  $(z^2\Omega\Delta z[n_e(t)/\tau_R])$ . Its integration over the time is the number of reemitted photons and can be used to replace the product of the first and the second factors in Equation (6). Therefore, the number of phonons received by the lidar during the integration time will be the following:

$$N_{He}^{Sat}(z) = N_{He}(z)\frac{1}{1 + (\tau_R/t_S)}\left\{1 - \frac{\tau_R}{\Delta t_L}\frac{(\tau_R/t_S)}{1 + (\tau_R/t_S)} \times \left[\exp\left(-\frac{\Delta t_L}{\tau_R}\left(1 + \frac{\tau_R}{t_S}\right)\right) - 1\right]\right\} + \frac{2N_B\tau\Delta z_{He}f}{c} \tag{15}$$

The saturation factor is defined as the ratio of backscattered photon counts with a saturation effect to those without a saturation effect. The lower the value of the saturation factor, the more pronounced the saturation effect becomes.

The saturation effect in resonance fluorescence lidar systems is profoundly influenced by laser pulse energy, altitude, pulse duration and beam divergence angle. Additionally,

the laser spectral bandwidth has a significant impact on the backscattering cross-section, further affecting the saturation effect. As depicted in Figure 7, the saturation effect becomes more pronounced as the pulse energy increases. Also, at a lower altitude, a more severe saturation effect happens.

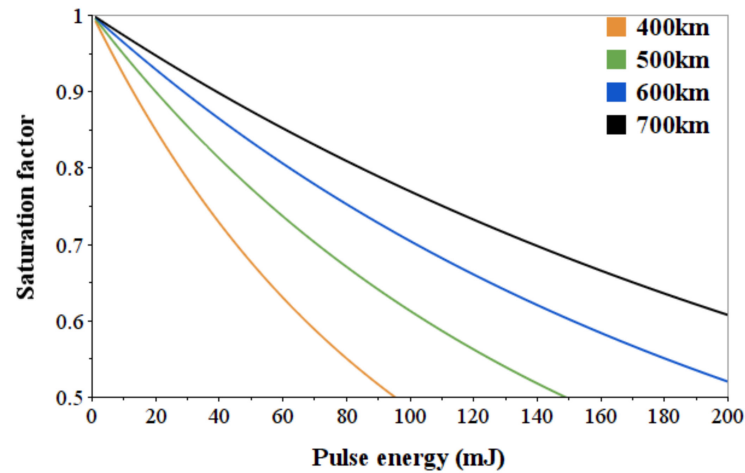


Figure 7. The impact of pulse energy on saturation effect at different altitudes (pulse duration is 10 ns, laser spectral bandwidth is 300 MHz, beam divergence angle is 33  $\mu$ rad).

Assuming that the saturation effect is negligible when the saturation factor exceeds 0.9, and considering a laser spectral bandwidth of 300 Hz, a pulse duration of 10 ns, and a beam divergence angle of 33  $\mu$ rad, the laser pulse energy must be less than 12 mJ, which leads to a maximum laser power of 0.6 when the repetition is 50 Hz.

#### 4.3. Simulation

Utilizing the parameters detailed in Table 1 and profiles of metastable helium number density in Figure 2, we conducted simulations to estimate the received photon counts (as shown in Figure 8) and SNR (as shown in Figure 9). It is notable that the SNR is dramatically affected by metastable helium number density.

Table 1. Parameters of pulsed lidar simulation.

Parameters		Value
Laser	Power	0.6 W
	Repetition	50 Hz
	Bandwidth	300 MHz
	Central wavelength	1083.03 nm
	Pulse duration	10 ns
Receiving optics	Telescope area	3.142 m <sup>2</sup>
	FOV	44 $\mu$ rad
Interference filter	Bandwidth	0.5 nm
	Peak transmittance	0.99
FPI	Bandwidth	4.6 GHz
	FSR	138 Ghz
	Peak transmittance	0.5
SNSPD	Dark counts	800 cps
	Quantum efficiency at 1083 nm	30%
Others	Integration time	1 h
	Range resolution	50 km
	One-way atmosphere transmittance	0.85 *

\* estimated from MODTRAN under excellent viewing conditions at a high-altitude site.

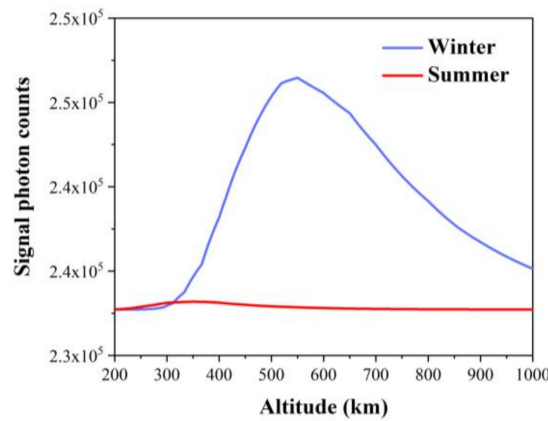


Figure 8. Total photon counts estimated in winter and summer.

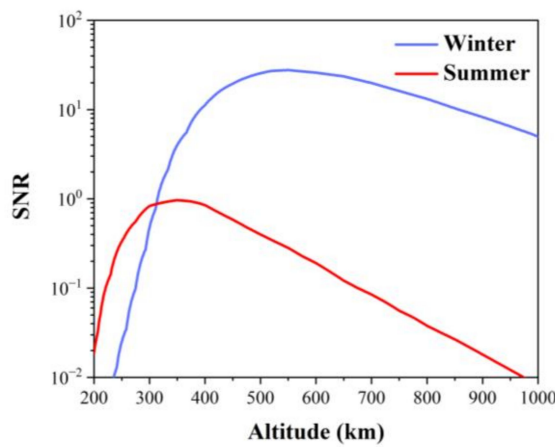


Figure 9. SNR estimated in winter and summer.

During the winter season, when metastable helium reaches its annual peak density, the SNR can soar to 27.5. Conversely, in the summer months, characterized by a significantly lower metastable helium atomic density, the achievable SNR is limited to approximately 1. At both the lowest and highest altitudes, the SNR diminishes substantially.

#### 4.4. Error Analysis

By normalizing the helium fluorescence signal to the Rayleigh signal, we effectively mitigate uncertainties stemming from our imprecise knowledge of pulse energy and system efficiency. However, it is essential to recognize that inaccuracies in the effective scatter cross-section can lead to systematic errors.

The effective scatter cross-section is equal to the convolution of the laser lineshape  $g_L$  and atomic scatter cross-section. We approximate the laser spectral lineshape by a Gaussian lineshape with a central frequency of  $\nu_L$  and an rms width of  $\sigma_L$ ; then,  $\sigma_{eff}$  is given by the following:

$$\sigma_{eff} = \int_{-\infty}^{\infty} \left( \sum_i^3 \sigma_i(\nu, \nu_0) \right) (g_L(\nu, \nu_L)) d\nu \tag{16}$$

where the subscript  $i$  corresponds to different radiation lines.  $\sigma_{eff}$  is affected by the temperature, vertical wind speed of the detected region and the central frequency of the laser.

Based on the error propagation principle,

$$\Delta\sigma_{eff}^2 = \sum_j \left( \frac{\partial\sigma_{eff}}{\partial X_j} \Delta X_j \right)^2 \tag{17}$$

where  $X_j$  stands for independent factors that can affect  $\sigma_{eff}$ . The relative uncertainty of  $\sigma_{eff}$  introduced by an individual factor can be expressed as  $\frac{\partial\sigma_{eff}}{\partial X_j} \frac{\Delta X_j}{\sigma_{eff}}$ , and this will be added in the quadrature. According to Equation (8), the relative error of atomic density introduced by  $\sigma_{eff}$  will be the same as the relative error of  $\sigma_{eff}$ .

To maintain laser frequency stability, a feedback control loop locks the laser frequency, limiting laser frequency shifts to within 20 MHz. The uncertainty introduced by this process is minimal, accounting for less than 0.3%.

Thermosphere temperatures fluctuate between 750 K and 1500 K, corresponding to solar minimum and solar maximum conditions, respectively. For our calculations, we use an average temperature of 1125 K. In this context, a temperature error of  $\pm 375$  K introduces an uncertainty of up to 6%.

In our calculations, we assume a vertical wind speed of 0, even though actual wind speeds of up to 100 m/s can be present. This introduces minor uncertainty of around 1% in our estimates.

Shot noise, which follows a Poisson distribution, governs the statistical fluctuations in photon counts. This means that the standard deviation of the total photon counts equals the square root of the photon counts themselves. In our measurements, the He signal is effectively normalized by the Rayleigh signal at lower altitudes, typically around 50 km. The Rayleigh signal is strong enough so that the photon noise contributed by the Rayleigh signal is negligible. The dominant error source is shot noise contributed by the weaker He signal. According to error propagation principles, the relative error induced by shot noise is the reciprocal of the SNR of the He signal.

Systematic errors considered in this paper, as well as errors introduced by shot noise in altitudes with the least relative error in different seasons, are listed in Table 2.

**Table 2.** Error analysis.

Error Factor	Value	Relative Error of Density
Laser central wavelength	1083.03 nm $\pm$ 0.08 pm	0.3%
Temperature	1125 K $\pm$ 375 K	6%
Wind speed	0 m/s $\pm$ 100 m/s	1%
Shot noise	550 km altitude in winter	3.6%
	350 km altitude in summer	103.5%

The various errors associated with the calibration process and photon-counting process are independent; according to the standard error propagation, the relative uncertainty of atomic number density they introduced can be added in the quadrature. The final relative error estimation is shown in Figure 10.

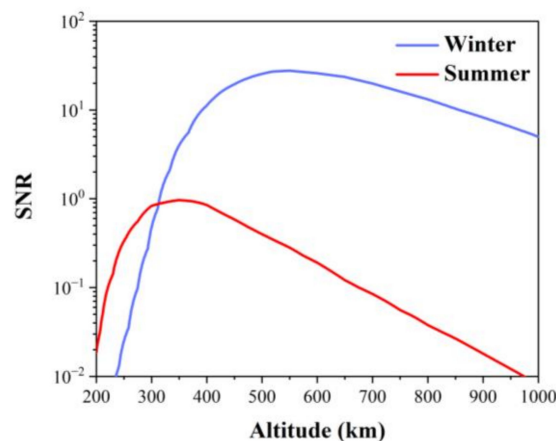


**Figure 10.** Total relative error.

During winter, when metastable helium is most abundant, the relative error in density above 370 km remains less than 20%. In contrast, during summer, when metastable helium is scarcer, the relative error is as high as 100%~200% at an altitude range of 270–460 km and even higher at other altitudes. These results demonstrate the feasibility and reliability of our metastable helium lidar system for density measurements.

## 5. Conclusions

In this paper, simulations were carried out to evaluate a pulsed lidar for metastable helium density measurement in the upper thermosphere and exosphere. The lidar system parameters were chosen based on the advancements in associated techniques, such as OPG and OPA technology and SNSPD. Simulations of return photon counts and relative errors at various altitudes are presented.

One of the primary focuses of the study is the discussion of saturation effects, which can lead to an underestimation of received signal counts and, further, an underestimation of metastable helium density. Based on the saturation effect, laser power has been optimized.

The simulations and error analyses conducted in the study validate the feasibility of the metastable helium lidar system for density measurements in the upper thermosphere and exosphere.

**Author Contributions:** Conceptualization, X.X. and D.S.; methodology, R.Z.; software, H.Z.; validation, Z.L.; formal analysis, J.L.; investigation, D.S.; resources, T.C.; data curation, Y.L.; writing—original draft preparation, J.L.; writing—review and editing, Y.H.; visualization, J.L.; supervision, Y.H.; project administration, X.X.; funding acquisition, X.X. All authors have read and agreed to the published version of the manuscript.

**Funding:** This research was funded by the National Natural Science Foundation of China (42125402, 42104146, 42374185), the Ground-based Space Environment Monitoring Network (the Chinese Meridian Project), the Innovation Program for Quantum Science and Technology (2021ZD0300301) and the Fundamental Research Funds for the Central Universities.

**Institutional Review Board Statement:** Not applicable.

**Informed Consent Statement:** Not applicable.

**Data Availability Statement:** Data underlying the results presented in this paper are not publicly available at this time but may be obtained from the authors upon reasonable request.

**Conflicts of Interest:** The authors declare no conflicts of interest.

## References

1. Christensen, A.; Patterson, T.; Tinsley, B. Observations and computations of twilight helium 10,830-Å emission. *J. Geophys. Res.* **1971**, *76*, 1764–1777. [[CrossRef](#)]
2. Tinsley, B.; Christensen, A. Twilight helium 10,830-Å calculations and observations. *J. Geophys. Res.* **1976**, *81*, 1253–1263. [[CrossRef](#)]
3. Kerr, R.; Noto, J.; Lancaster, R.; Franco, M.; Rudy, R.; Williams, R.; Hecht, J. Fabry Perot observations of helium 10830 Å emission at Millstone Hill. *Geophys. Res. Lett.* **1996**, *23*, 3239–3242. [[CrossRef](#)]
4. Young, A.T. Rayleigh scattering. *Phys. Today* **1982**, *35*, 42–48. [[CrossRef](#)]
5. She, C.-Y. Spectral structure of laser light scattering revisited: Bandwidths of nonresonant scattering lidars. *Appl. Opt.* **2001**, *40*, 4875–4884. [[CrossRef](#)] [[PubMed](#)]
6. Gerding, M.; Wing, R.; Franco-Diaz, E.; Baumgarten, G.; Fiedler, J.; Köpnick, T.; Ostermann, R. The Doppler wind, temperature, and aerosol RMR lidar system at Kühlungsborn/Germany—Part 1: Technical specifications and capabilities. *EGU Sphere* **2023**, *2023*, 1–29. [[CrossRef](#)]
7. Baumgarten, G. Doppler Rayleigh/Mie/Raman lidar for wind and temperature measurements in the middle atmosphere up to 80 km. *Atmos. Meas. Tech.* **2010**, *3*, 1509–1518. [[CrossRef](#)]
8. Khaykin, S.M.; Hauchecorne, A.; Wing, R.; Keckhut, P.; Godin-Beekmann, S.; Porteneuve, J.; Mariscal, J.-F.; Schmitt, J. Doppler lidar at Observatoire de Haute-Provence for wind profiling up to 75 km altitude: Performance evaluation and observations. *Atmos. Meas. Tech.* **2020**, *13*, 1501–1516. [[CrossRef](#)]
9. Bowman, M.R.; Gibson, A.J.; Sandford, M.C.W. Atmospheric Sodium measured by a Tuned Laser Radar. *Nature* **1969**, *221*, 456–457. [[CrossRef](#)]
10. Pfrommer, T.; Hickson, P. High-resolution lidar observations of mesospheric sodium and implications for adaptive optics. *JOSA A* **2010**, *27*, A97–A105. [[CrossRef](#)]

11. Granier, C.; Jegou, J.P.; Megie, G. Iron atoms and metallic species in the Earth's upper atmosphere. *Geophys. Res. Lett.* **1989**, *16*, 243–246. [[CrossRef](#)]
12. Collins, R.; Li, J.; Williams, B.; Kaifler, B.; Thorsen, D. All-Solid State Iron Resonance Lidar for Measurement of Temperature and Winds in the Upper Mesosphere and Lower Thermosphere. In *International Laser Radar Conference*; Springer International Publishing: Cham, Switzerland, 2022; pp. 189–195.
13. Felix, F.; Keenlside, W.; Kent, G.; Sandford, M.C.W. Laser Radar Observations of Atmospheric Potassium. *Nature* **1973**, *246*, 345–346. [[CrossRef](#)]
14. Feng, W.; Höffner, J.; Marsh, D.; Chipperfield, M.; Dawkins, E.; Viehl, T.; Plane, J. Diurnal variation of the potassium layer in the upper atmosphere. *Geophys. Res. Lett.* **2015**, *42*, 3619–3626. [[CrossRef](#)] [[PubMed](#)]
15. Gerrard, A.J.; Kane, T.J.; Meisel, D.D.; Thayer, J.P.; Kerr, R.B. Investigation of a resonance lidar for measurement of thermospheric metastable helium. *J. Atmos. Sol. -Terr. Phys.* **1997**, *59*, 2023–2035. [[CrossRef](#)]
16. Carlson, C.G.; Dragic, P.D.; Price, R.K.; Coleman, J.; Swenson, G.R. A narrow-linewidth, Yb fiber-amplifier-based upper atmospheric Doppler temperature lidar. *IEEE J. Sel. Top. Quantum Electron.* **2009**, *15*, 451–461. [[CrossRef](#)]
17. Mangogna, A.D. *Helium Resonance Fluorescence LiDAR*; University of Illinois at Urbana-Champaign: Champaign County, IL, USA, 2015.
18. Kaifler, B.; Geach, C.; Büdenbender, H.C.; Mezger, A.; Rapp, M. Measurements of metastable helium in Earth's atmosphere by resonance lidar. *Nat. Commun.* **2022**, *13*, 6042. [[CrossRef](#)] [[PubMed](#)]
19. Cai, Y.; Sun, D.; Xue, X.; Zheng, J.; Lan, J.; Li, Z.; Zhang, N.; Dou, X. Parameter design and performance analysis of lidar system for thermospheric helium. *Chin. J. Lasers* **2017**, *44*, 910001.
20. Pan, T.; Sun, D.; Zhao, R.; Lan, J.; Han, Y.; Chen, T.; Xue, X.; Tang, L. Parameter design and performance analysis of bistatic helium lidar system. *Acta Photonica Sin.* **2019**, *48*, 1001001.
21. Bishop, J.; Link, R. Metastable He 1083 nm intensities in the twilight: A reconsideration. *Geophys. Res. Lett.* **1993**, *20*, 1027–1030. [[CrossRef](#)]
22. Bishop, J.; Link, R. He (23 S) densities in the upper thermosphere: Updates in modeling capabilities and comparisons with midlatitude observations. *J. Geophys. Res. Space Phys.* **1999**, *104*, 17157–17172. [[CrossRef](#)]
23. Hodgman, S.S.; Dall, R.G.; Byron, L.J.; Baldwin, K.G.H.; Buckman, S.J.; Truscott, A.G. Metastable Helium: A New Determination of the Longest Atomic Excited-State Lifetime. *Phys. Rev. Lett.* **2009**, *103*, 053002. [[CrossRef](#)] [[PubMed](#)]
24. Shefov, N.N. Helium in the upper atmosphere. *Planet. Space Sci.* **1963**, *10*, 73–77. [[CrossRef](#)]
25. Fujii, T.; Fukuchi, T. *Laser Remote Sensing*; CRC Press: Boca Raton, FL, USA, 2005.
26. Waldrop, L.; Kerr, R.; Gonzalez, S.; Sulzer, M.; Noto, J.; Kamalabadi, F. Generation of metastable helium and the 1083 nm emission in the upper thermosphere. *J. Geophys. Res. Space Phys.* **2005**, *110*. [[CrossRef](#)]
27. Bhuiyan, A.; Richardson, D.; Naik, S.; Lucht, R. Development of an optical parametric generator with pulsed dye amplification for high-resolution laser spectroscopy. *Appl. Phys. B* **2009**, *94*, 559–567. [[CrossRef](#)]
28. Pan, T.; Chen, T.; Sun, D.; Han, Y.; Xue, X.; Zhao, R.; Lan, J. Metastable helium Faraday filter for helium lidar to measure the density of the thermosphere. *Opt. Express* **2021**, *29*, 4431–4441. [[CrossRef](#)] [[PubMed](#)]
29. Chen, Q.; Zhang, B.; Zhang, L.; Ge, R.; Xu, R.; Wu, Y.; Tu, X.; Jia, X.; Pan, D.; Kang, L.; et al. Sixteen-Pixel NbN Nanowire Single Photon Detector Coupled With 300- $\mu$ m Fiber. *IEEE Photonics J.* **2020**, *12*, 2954938. [[CrossRef](#)]
30. Zhang, B.; Guan, Y.-Q.; Xia, L.; Dong, D.; Chen, Q.; Xu, C.; Wu, C.; Huang, H.; Zhang, L.; Kang, L.; et al. An all-day lidar for detecting soft targets over 100 km based on superconducting nanowire single-photon detectors. *Supercond. Sci. Technol.* **2021**, *34*, 34005. [[CrossRef](#)]
31. Welsh, B.M.; Gardner, C.S. Nonlinear resonant absorption effects on the design of resonance fluorescence lidars and laser guide stars. *Appl. Opt.* **1989**, *28*, 4141–4153. [[CrossRef](#)]
32. Milonni, P.W.; Fugate, R.Q.; Telle, J.M. Analysis of measured photon returns from sodium beacons. *J. Opt. Soc. Am. A* **1998**, *15*, 217–233. [[CrossRef](#)]
33. Von der Gathen, P. Saturation effects in Na lidar temperature measurements. *J. Geophys. Res. Space Phys.* **1991**, *96*, 3679–3690. [[CrossRef](#)]
34. Milonni, P.W.; Fearn, H.; Telle, J.M.; Fugate, R.Q. Theory of continuous-wave excitation of the sodium beacon. *J. Opt. Soc. Am. A* **1999**, *16*, 2555–2566. [[CrossRef](#)]

**Disclaimer/Publisher's Note:** The statements, opinions and data contained in all publications are solely those of the individual author(s) and contributor(s) and not of MDPI and/or the editor(s). MDPI and/or the editor(s) disclaim responsibility for any injury to people or property resulting from any ideas, methods, instructions or products referred to in the content.